# Microscopic stress analysis of nanoscratch induced sub-surface damage in a single-crystal silicon wafer

Ning Huang[1], Ping Zhou[1] and Saurav Goel[2,3]

[1]Key Laboratory for Precision and Non-traditional Machining Technology of Ministry of Education, Dalian University of Technology, Dalian 116024, China

[2] School of Engineering, London South Bank University, 103 Borough Road, London SE1 0AA, UK

[3] University of Petroleum and Energy Studies, Dehradun, 248007, India

Corresponding author: pzhou@dlut.edu.cn

**Abstract**

The existing stress criterion assumes the material to be isotropic and only distinguishes elastic, plastic and crack zones to explain the scratching-induced sub-surface damage (SSD) during the contact loading processes such as nanoindentation, nanoscratching and grinding. However, anisotropic single-crystal materials such as monocrystalline silicon and silicon carbide have more diverse defect characteristics and SSD in these materials cannot be well explained and predicted using the existing criterion. In this study, a thorough microscopic characterisation and complementary stress analysis were performed on a single-crystal silicon wafer during nanoscratching. A novel criterion based on mechanism of dislocation multiplication and propagation was proposed and validated, providing a better understanding of SSD prediction in silicon. Compared to conventional SSD models, this new shear stress-based criterion can accurately predict the position and extent of dislocations in silicon. The dislocations layout for scratching along any direction on the (100) surface of Si were further discussed to offer a comprehensive understanding of the effect of anisotropic structure of single-crystals on the SSD. The improved understanding of inelastic deformation in single-crystal silicon, which was revealed by this new model, will have a significant impact on the nanomanufacturing

sector by guiding the contact mode experiments (grinding, indentation, machining) towards efficient machining.

**Keywords:** Single-crystal silicon; stress criterion; scratch test; sub-surface damage; crystalline defect

**Abbreviations**

| | |
|---|---|
| **α** : | Boussinesq stress field |
| **β** : | Cerruti stress field |
| **γ** : | Residual blister stress field |
| $E$ : | Elastic modulus |
| $H$ : | Hardness |
| $\varphi$ : | Half included angle of the tool |
| $F_n$ : | Normal load |
| $K_c$ : | Fracture toughness |
| $b$ : | Half of inelastic zone width |
| $v$ : | Poisson's ratio |
| $\sigma_y$ : | Yield strength |
| SSD: | Sub-surface damage |
| ECM: | Expanding cavity model |
| ECCM: | Expanding cylindrical cavity model |

## 1. Introduction

The demand for precision machining of single-crystal silicon is expected to grow at a compound annual growth rate (CAGR) of 9.53% over the next 5 years (2022-2027) [1].

This is because silicon is among the most widely used semiconductors in various microelectronic applications such as integrated circuits and Photovoltaic (PV) solar cells. Industrially grown wafers of silicon are often subjected to an ultra-precision grinding operation [2] to shape them to the desired sizes.

However, a grinding process inevitably induces defects in the machined sub-surface of the wafer often referred to as sub-surface damage (SSD), which leads to poor surface integrity and inferior electro-mechanical performance. SSD can further compromise the fatigue life, optical performance and thermal performance [3] of the ground component and therefore these defects need to be eliminated by carrying out polishing as a post-grinding operation. The larger the extent of these defects, the more is the extent of post-grinding polishing. Therefore, an insight into understanding the nature of these defects with a view to reduce their extent during grinding can help achieve sustainability during precision grinding.

Hitherto, many attempts have been made using molecular dynamics simulations [4][5], finite element analysis [6] and atomic force microscope (AFM) experiments [7] to get clarity on these aspects but the mismatch of length/time scale and lack of instruments to directly monitor the sub-surface defects in real time has resulted in a limited progress on this topic. Consequently, the development of a reliable model to predict SSD during grinding has remained a frontal manufacturing challenge in the field of micro/nano scale processing of brittle materials.

Single grit scratching is an ideal representation of a contact loading problem, such as grinding. The damage mechanisms that occur during single-grit scratching can provide fundamentally important and new insights into the sub-surface integrity [8]. The deformation mechanisms in single-crystal silicon during scratch tests have been studied extensively in the literature [9][10][11]. Cross-sectional examination of single-crystal silicon during indentation [12] and scratch tests [10] shows that SSD can involve several events depending on the stress levels experienced by the location and depending on the material being ground, including phase transformation, stacking faults, slip bands and micro-cracks [13].

At lower loads, the plastic zone may only consist of a phase transformation zone [14]. It is now understood that the occurrence of metastable phase transformation in silicon, leading to its amorphisation, is key to exploit ductility in silicon which results in the commonly known brittle-ductile transition [11]. As the load increases, dislocations nucleate at the boundary of the phase transformation zone [15] and penetrate into the bulk material along specific crystal directions, forming slip bands. As a result, slip bands can usually be observed at an angle of 54.7° to the scratch surface in TEM samples of scratches on the (001) surface of silicon, when the incident electron beam is kept parallel to the <110> direction, which is the angle between the {100} plane and the {111} plane [14]. Researchers have also reported on the critical threshold for dislocation nucleation in silicon [16], and the Schmid factor is often used to evaluate the likelihood of activating slip systems in a particular orientation [17]. As the load further increases, dislocation accumulation at the intersections of dislocations, such as L-C locks can result in the formation of median cracks, which release the critical loading energy and define the maximum depth of sub-surface damage. Therefore, accurately predicting the depths of various types of damage is an essential foundation for precision grinding process research.

Analytical models have been proposed using fracture mechanics approaches to correlate normal load and crack depth. The expanding cavity model (ECM), developed from scratches and indentations, is a primitive effort for understanding the inelastic response of brittle materials. It was postulated that a hemispherical plastic zone engulfed by the contact area creates a stress field that drives ensuing cracks [18]. Lambropoulos *et al.* [19] established the relationship between median crack depth and normal force based on fracture mechanics. Jing *et al.* [20] modified the expanding cylindrical cavity model (ECCM) for predicting the size of the plastic zone beneath a single abrasive scratch and the depth of lateral cracks by introducing the Blister stress field. On the basis of Lambropoulos's model and Jing's model, several researches [21][22][23] have reported an SSD prediction model for the grinding process wherein attempts were made to (i) derive normal load as a function of grit penetration depth using classical indentation hardness theory, (ii) substitute the relationship between normal force and indentation depth into the models to obtain SSD depth as a function of cutting depth during single-grit scratching, and (iii) perform grinding kinematics analysis to establish the SSD prediction model.

However, cracks are assumed to generate underneath the plastic zone in the classical ECM, while in single-crystal silicon, cracks emanate at the intersections of crystalline defects. Therefore, the applicability of the classical crack depth model in single-crystal silicon remains to be investigated. Additionally, current models on single-grit damage are typically based on quasistatic loading involving low velocities, around 1 μm/s. Considering the strong impact of strain rate on dynamic hardness and fracture toughness, it remains to be determined whether these models are valid for anisotropic materials during high strain-rate deformation such as in grinding.

Attempts have been made to consider the effect of material anisotropy by substituting the average Young's modulus and Poisson's ratio from various crystal orientations [24][25], as the blister stress field equation include material property parameters. However, there is a limitation of the ECCM approach when considering material anisotropy in this model, as the plastic zone is assumed to be semi-cylindrical in ECCM, i.e. the material is isotropic, which clearly differs from the crystallographic orientation-dependent plastic behaviour of anisotropic materials, including the generation and propagation of slip bands into the interior of the material along specific directions [12]. This points us to the drawback of the ECCM model and raises a key question whether Jing' model is still applicable to estimate the size of the plastic zone in anisotropic materials like silicon. This question becomes pertinent because to the best of the authors' knowledge, none of the existing analytical models consider anisotropy of inelastic deformation of the material. Besides, there is currently no experimental evidence that provides a direct estimate of the position and extent of dislocation propagation in silicon based on a given crystallographic orientation during contact loading.

Based on the literature review, this research paper aims to address the following questions:

(i) Can the depth of dislocation nucleation be predicted during a scratch tests in an anisotropic brittle material? If so, will the dislocation depth and distribution be the same or different for scratching along different crystallographic orientations under the same load?

(ii) Can currently available prediction models be reliably used for anisotropic materials such as nanocrystalline silicon? If not, what aspect needs to be further considered to make these models robust?

(iii) Can the quasi-static stress field based on the scratch load be used reliably to analyse the extent and nature of defects in a dynamic cutting process such as grinding?

To answer these questions, nanoscratching experiments were used in conjunction with engineering analysis and microscopic imaging using advanced microscopic imaging tools such as AFM and TEM to elucidate refreshing new insights into the sub-surface mechanisms in single-crystal silicon. In the discussion section, we have made specific observations on five main points which are (i) directional dependence of amorphisation, (ii) maximum depth of the dislocation during scratching, (iii) maximum depth of the phase-transformed layer, (iv) maximum depth of median crack, and (v) width of the inelastic zone. This paper is expected to provide a guide for gaining a better understanding of the material deformation mechanisms and processing science of single-crystal silicon.

## 2. Experimental setup and methodology

The scratch tests were conducted on the (001) surface of a commercially available 8-inch p-type monocrystalline silicon wafer using a custom-made scratching apparatus [26]. The rotary motion of the wafer around its own axis allowed for a scratching speed of up 5 m/s, which mimics an actual grinding operation. A protruded area with a curved profile on the wafer shown in Figure 1(a) was chosen for scratching to ensure that scratches were performed with ramped depth-of-cut for measurable scratch length and load. A diamond Berkovich tip with a tip radius of 850 nm was fed radially along the wafer at regular intervals to make parallel wear tracks to avoid duplicate cuts, as illustrated in Figure 1(b)~(c). The tip remained static during the contact with the workpiece, so the scratching method used in this paper is essentially passive depth-control. The spacing of the two adjacent scratches was maintained at 2 μm to avoid interference and to ensure that the post-scratching inspection of a single lamella captures all scratches for achieving consistency in comparison as shown in Figure 1(d).

Detailed experimental parameters are shown in Table 1. An atomic force microscope (XE200, Park systems, Korea) was used to measure the scratched surface using the tapping mode function. Post-scratching characterization was carried out using transmission electron microscopy (TEM) (Talos F200X, Fei, America) and focused ion beam (FIB) (Helios, FEI, America), as per the scheme shown in Figure 1(d). Prior to FIB, the scratched samples were coated with a polymer film to protect the surface structure from radiation damage of gallium ion. During TEM, the incident electron beam was kept parallel to the [110] direction, unless otherwise stated.

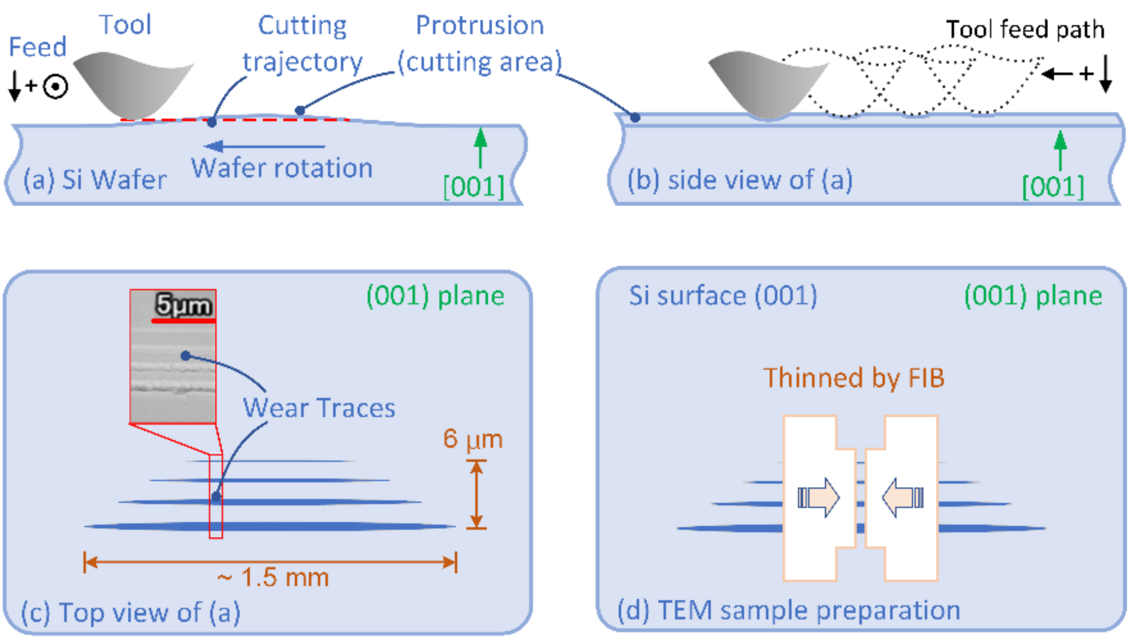


Figure 1. Schematic illustration of the scratch method (a)~(c) showing wear traces with nanoscale ramping depth-of-cut and the sample preparation method (d) denoting the area on the scratched region being chosen for the cross-sectional TEM observation.

Table 1 Experimental parameters used for scratching silicon

| Sample | Velocity (m/s) | Scratch direction | Number of scratches |
|---|---|---|---|
| A | 0.1 | (001)[110] | 4 |
| B | 1 | (001)[110] | 4 |
| C | 1 | (001)[010] | 4 |

## 3. Results and discussions

### *3.1 Directional dependent amorphisation*

The AFM and cross-sectional TEM micrographs of residual scratches are depicted in Figure 2. Both topography and TEM images in Figure 2 show that regardless of the scratch speed, the material was squeezed to both sides of the groove, indicating that the scratches were produced by plastic deformation, and that the material removal occurred fully in the ductile-mode [27].

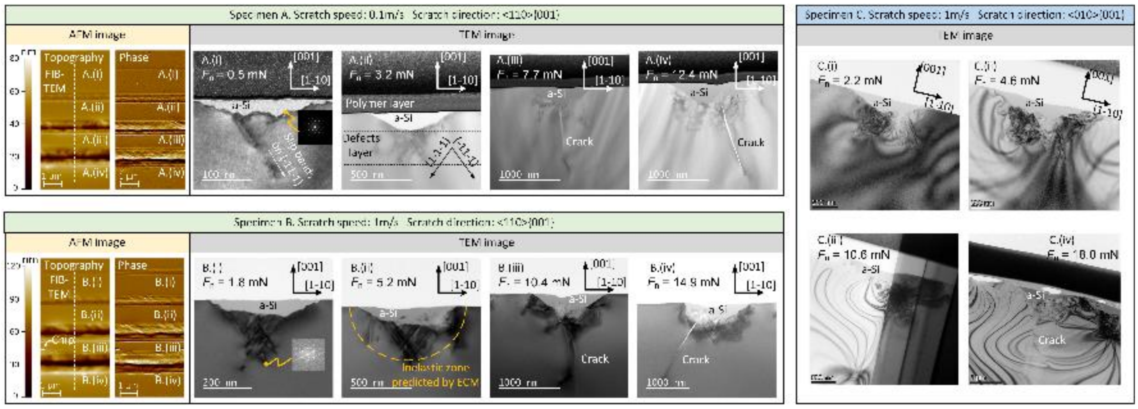


Figure 2. Scratch topographies inspected by AFM under tapping mode and corresponding detailed TEM observations of sub-surface defects in specimens A, B, and C. The scratches are numbered as A.(i)~A.(iv), B.(i)~B.(iv) and C.(i)~ C.(iv) to clearly show the TEM micrographs at various loads.

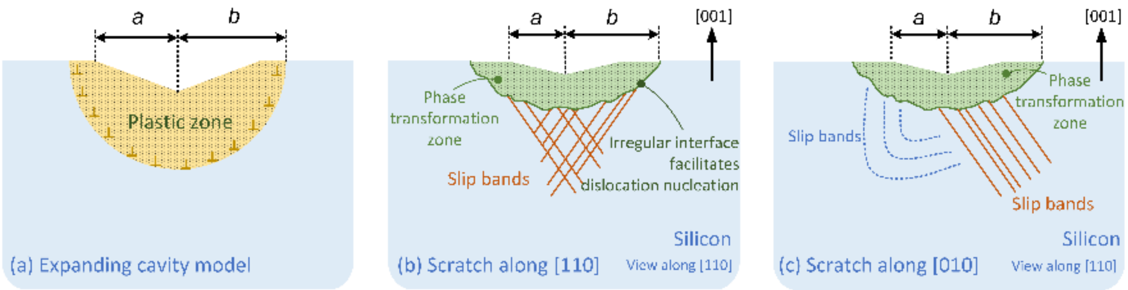


Figure 3. Schematics of scratch groove sub-surface structure in (a) conventional expanding cavity model, (b) [110] scratch in single-crystal silicon and (c) [010] scratch in single-crystal silicon. Solid lines in (b) and (c) denote slip bands on {111} slip planes viewed edge-on and dashed and dotted lines in (c) denote slip bands on {111} slip planes oblique to the [110] projection.

From the TEM micrographs, the sub-surface deformation of silicon can be seen to have a directional dependence, as well as a plastic zone and stacking faults generated underneath amorphous silicon, which are visible as non-equidistant from the axi-symmetric centre of the indenter in contrast to the semi-cylindrical plastic zone assumed in the expanding cylindrical cavity model (Hertz theory) highlighted in Figure 3.

The TEM results of the scratched specimens revealed two distinct zones, namely, (i) the phase-transformed region at the upper zone of the sub-surface region, and (ii) the boundary between the amorphous and single-crystal region, which appears to be an irregular surface undergoing partial transformation due to differential stress gradients such that the nucleated dislocations extending into the interior of the material in the {111} planes remain entrapped after unloading. Tang *et al.* [28] suggested that these defects are spaced at different intervals as a result of inhomogeneous stress distributions. A few vertical stacking faults perpendicular to the (100) surface were activated (A(ii)~A(iv), B(ii)~B(iv)) due to the increased stress levels. The distribution of slip bands in sample C was different from that of sample A and B, as schematically illustrated in Figure 3. This difference is discussed in more detail in the next section on dislocations and slip bands.

*3.2 Depth of dislocations*

TEM observations on silicon lamella from Figure 2, as well as from the previously reported indentation [12] and scratch [10] studies on single-crystal silicon samples have shown that the penetration of dislocations into the bulk material within the slip plane is responsible for determining the depth of the plastically deformed zone. According to the well-known Peierls-Nabarro model of dislocations [29], the displacement of a dislocation is closely related to the stress components within the slip plane, because dislocations must overcome an energy barrier to propagate through the lattice. The force required to overcome this resistance is known as *Peierls-Nabarro (P-N)* stress, which varies sinusoidally with respect to the displacement of the dislocation.

However, it is acknowledged that the calculation of P-N stress is inaccurate according to Meyers [30], due to the failure of continuum theory at the atomic level (lattice spacing). Therefore, a hypothesis is proposed that the tendency of dislocations to move through a crystal can be described by the stress acting on the dislocation line, and that there exists a critical resolved shear stress, which is the deviatoric component of the applied stress resolved on the slip plane. If the resolved shear stress drops below this critical value, the dislocation cannot propagate. Since the exact value of this critical stress cannot be calculated theoretically, it is suggested that scratching experiments be conducted to determine an experimental-based critical shear stress by evaluating the shear stress at the spatial point where a dislocation terminates. With this critical value, the depth of dislocations induced by mechanical loading can be predicted using theoretically calculated shear stress contours."

Peach-Koehler equation [30] defines the force F acting on a dislocation line as follows:

$$\mathbf{F}=(\boldsymbol{\sigma}\cdot\mathbf{b})\times\mathbf{l} \tag{1}$$

where $\boldsymbol{\sigma}$ is the local stress field, $\boldsymbol{b}$ is the burgers vector, and $\boldsymbol{l}$ is the local dislocation line tangent direction. It should be noted that the force $\boldsymbol{F}$ in Eq. (1) is not a physical force, but rather a means of describing the tendency of a dislocation to move when stresses are present. Eq. (1) shows that the stress components that contribute to the movement of a dislocation depend on factors including the Burgers vectors, the direction of the dislocation lines, and the type of dislocation. Therefore, it is crucial to accurately identify the crystallographic properties of dislocations induced by mechanical stresses in order to determine which stress component is associated with the movement of the dislocation.

Danilewsky *et al.* [31] and Hänschke *et al.* [32] provided a conclusive picture of three-dimensional slip-band arrangements through the use of correlated x-ray diffraction imaging and light microscopy. Their observations showed that the dislocation loops emerged into four {111}-planes underneath the indenter during loading (see **Error! Reference source not found.**). Each inclined {111} slip plane consists of half-hexagonal dislocation loops that multiplies and spread around the scratch, and each dislocation loop consists of two inclined 60° and one screw dislocation with a Burgers vector of $a/2\langle 110\rangle$ (with lattice constant $a$). The color code for planes in **Error! Reference source not found.** illustrates the {111} slip planes around scratch on the (001) surface and the color code for lines in **Error! Reference source not found.**(b) denotes Burgers vector orientations for dislocations with maximum depth. These dislocations were of screw type because the external force generates resolved shear stresses within these slip planes that cause clockwise and anticlockwise rotation on the surface normal [33].

According to Eq. (1), shear stress components on the slip plane in the direction of **b** contribute to the gliding force for screw dislocation movement. Therefore, it is natural to believe that when the shear stress in the {111} slip plane along <110> direction, i.e. $\tau_{\{111\}<110>}$, drops to a critical value, the depth corresponding to this shear stress denotes the maximum depth of the dislocation movement during the scratching of silicon.

To verify the above hypothesis, we estimated and obtained the shear stress $\tau_{\{111\}<110>}$ on the four {111} planes (coloured) using analytical calculations. We utilized the work of Jing *et al*. [20], whose results suggest that the stress field **σ** in the crystalline zone during single-grit scratch tests can be constructed as a superposition of the Boussinesq stress field **α**, formed by the normal point force, the Cerruti stress field **β**, formed by the tangential point force, and the sliding blister field **γ**, formed by the phase transformed layer above the crystal defects:

$$\sigma_{ij} = \alpha_{ij} + k_1 \beta_{ij} + k_2 \gamma_{ij} \tag{2}$$

$$k_2 = f \frac{3\lambda^2}{4\pi^2 (1-2v)(1+v)} \frac{E}{H} \cot \alpha \tag{3}$$

where subscripts $i$ and $j$ represent the direction of the stress component, $k_1$ is the coefficient of friction, $k_2$ is the coefficient of the sliding blister field in the phase transitioned region, and $\lambda$ is a geometric factor ($\lambda$=1 for an axisymmetric indenter). Here, a value of the coefficient *as* $k_1$=0.5 was used [16].

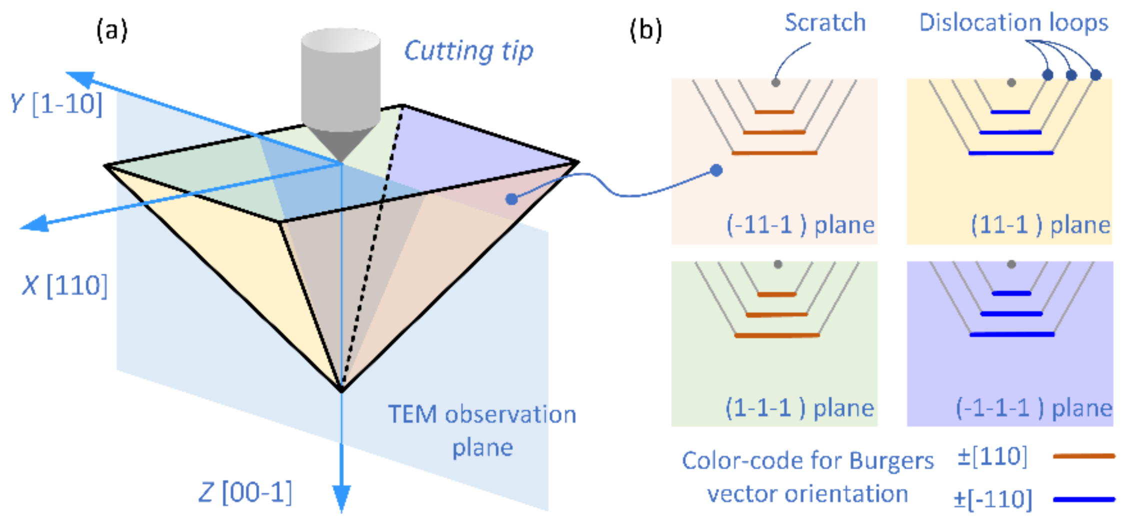


Figure 4. Schematic of (a) formation of slip bands from dislocation loops during scratching and (b) multiplication and propagation of dislocation loops on the {111} slip plane. Each half loop consists of two inclined 60° and one screw dislocation with a Burgers vector orientation of <110>.

Two simplifications should be noted regarding Eq. (3). (i) The value of $f \times E/H$ in Eq. (3) was suggested to be 1.09 for a sharp indenter by Cook and Pharr [34], and as a result, the coefficient $k_2$ was considered as 0.1, indicating that the sliding blister field only accounts for a very small fraction of stress. Additionally, the residual stress of the phase transformed layer is several orders of magnitude smaller than the stress caused by scratch load [35]. Therefore, the sliding blister stress field $\gamma$ caused by the phase transformed zone has not been considered in this paper. Jing *et al.* [20] derived expression for $\alpha_{ij}$ and $\beta_{ij}$ in the cartesian coordinate system. The relevant derived expressions are provided in detail in Appendix A. (ii) The anisotropy of single crystal silicon, as a crystalline material, is taken into account in this paper by analysing the slip motion of dislocation loops on slip planes. However, for the purpose of stress field calculations, we adopted an isotropic material assumption as stated in Eq. (2) to simplify the analytical calculation of the stress field. A dummy finite element analysis was conducted and it was found that the error introduced by this simplification is negligible.

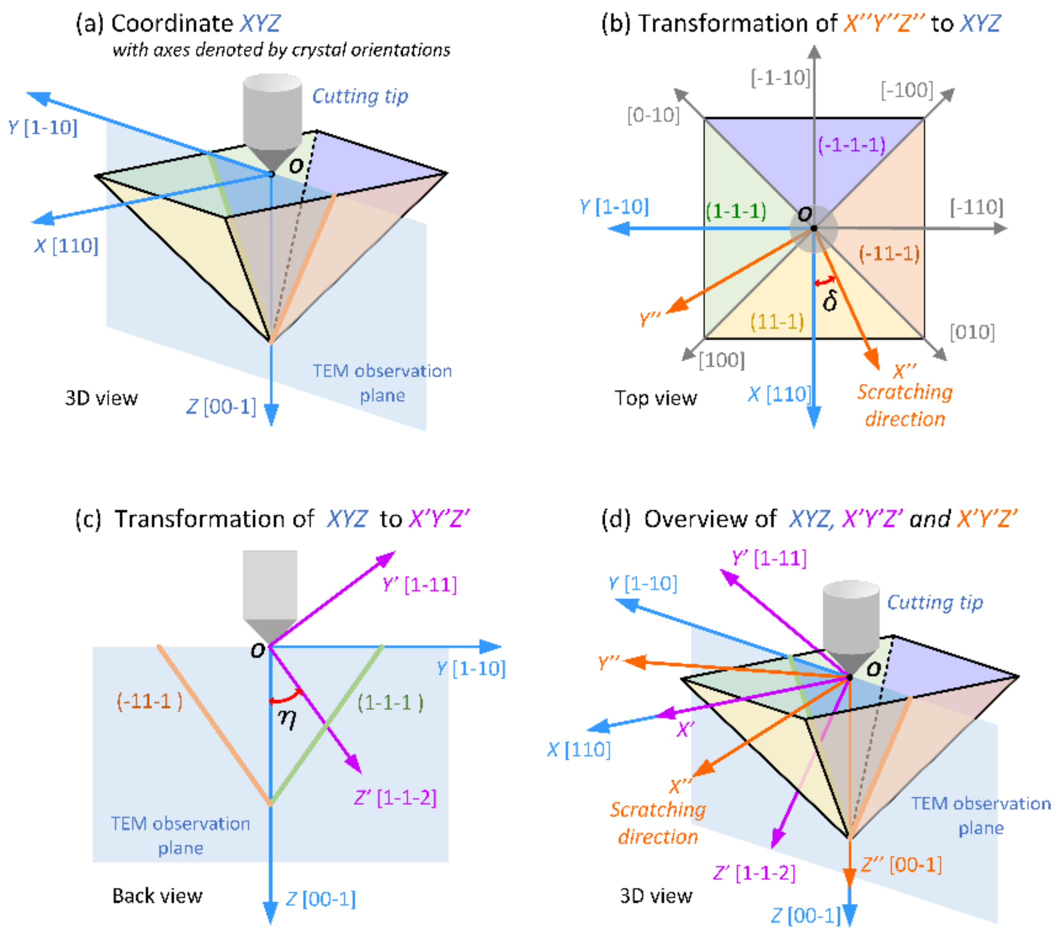


Figure 5. Schematics of (a) coordinate *XYZ* denoted by crystal orientation, (b)-(c) coordinate transformation, and (d) overview of three coordinate systems. The stress field **σ** is first transformed from the scratch coordinate system *X″Y″Z″* to a fixed intermediate coordinate system *XYZ* by rotating it by an angle $\delta$ around the $Z''$ axis, which is followed by a rotation around the $X$ axis by angle $\eta$, resulting in the transformed coordinate system *X′Y′Z′*.

The scratch direction $OX''$ denoted by the orange arrow in Figure 5 can be set to any direction on the (001) wafer surface to consider material's anisotropy, with the variable $\delta$ in Figure 5 defining the angle between the scratch direction $OX''$ and the x-axis ([110] direction). Note that the stress field **σ** calculated by Eq. (2) is established in the coordinate system $X''Y''Z''$ (hereafter would be referred as scratch coordinate), since $OX''$ denotes the scratch direction. To obtain the stress component $\tau_{\{111\}<110>}$, the stress coordinate $X'Y'Z'$ is introduced, with the $X'OZ'$ plane denoting the {111} plane and $OY'$ axis denoting the <110> direction, as shown in Figure 5. The stress field $\boldsymbol{\sigma}$ is then transformed from the scratch coordinate $X''Y''Z''$ to the stress coordinate $X'Y'Z'$ using

$$\boldsymbol{\sigma}' = \mathbf{T} \cdot \boldsymbol{\sigma} \cdot \mathbf{T}^{T} \tag{4}$$

where $\boldsymbol{T}$ is the transformation matrix. An intermediate coordinate system $XYZ$ was introduced to facilitate the calculation of the matrix $\boldsymbol{T}$ with the following steps: (i) the scratch coordinate system $X''Y''Z''$ is first rotated around the $Z''$ axis by an angle $\delta$, resulting in the fixed intermediate coordinate system $XYZ$, as shown in Figure 5(b). (ii) Then the intermediate coordinate system is rotated around the $X$ axis by an angle $\eta$, resulting in the stress coordinate system $X'Y'Z'$. The angle $\eta$ can be determined by calculating the angle between the Z-axis [00-1] and the Z'-axis [1-1-2], as illustrated in Figure 5(c). By using this intermediate coordinate system $XYZ$, Eq. (4) can be rewritten as:

$$\boldsymbol{\sigma}' = \mathbf{T}_2 \cdot \mathbf{T}_1 \cdot \boldsymbol{\sigma} \cdot \mathbf{T}_1^{T} \cdot \mathbf{T}_2^{T} \tag{5}$$

where $\boldsymbol{T}_1$ and $\boldsymbol{T}_2$ are transformation matrices for $X''Y''Z''$-to-$XYZ$ and $XYZ$-to-$X'Y'Z'$ respectively. The elements of matrix $\boldsymbol{T}_1$ was defined in terms of direction cosines of the angles between scratch coordinate axes $OX''$, $OY''$, $OZ''$ and intermediate coordinate axes $OX$, $OY$, $OZ$:

$$\mathbf{T}_1 = \begin{pmatrix} \cos\delta & \sin\delta & 0 \\ \sin\delta & \cos\delta & 0 \\ 0 & 0 & 1 \end{pmatrix} \tag{6}$$

Similarly, the elements of matrix $\boldsymbol{T}_2$ were defined in terms of direction cosines of the angles between intermediate coordinate axes $OX$, $OY$, $OZ$ and transformed coordinate axes $OX'$, $OY'$, $OZ'$. As the direction of these coordinate axes are defined by the crystalline orientation, the transformation matrix $\boldsymbol{T}_2$ for (-11-1) plane was calculated as:

$$\mathbf{T}_2 = \begin{pmatrix} 1 & 0 & 0 \\ 0 & \dfrac{\sqrt{3}}{3} & -\dfrac{\sqrt{6}}{3} \\ 0 & \dfrac{\sqrt{6}}{3} & \dfrac{\sqrt{3}}{3} \end{pmatrix} \tag{7}$$

Using Eq. (2)~(7), the shear stress $\tau_{(-11-1)[110]}$ can be calculated at any point in the space beneath the scratch tip. Similarly the shear stress $\tau_{(1-1-1)[110]}$ can also be obtained. It is noteworthy to learn that the behaviour of the slip bands on (-11-1) and (1-1-1) cannot be predicted from the stress field of the cutting tip at a particular position, as the stress field within the TEM observation plane (the blue plane in Figure 5) varies continuously with the cutting tip position during the scratching process. To reveal the relationship between the shear stress and the slip bands consisting of dislocation loops, we calculated the peak values of shear stresses $\tau_{(-11-1)[110]}$ and $\tau_{(1-1-1)[110]}$ (hereafter referred as peak stress) in the TEM observation plane as the tip scratch across this plane, and further compared the stress contours of peak stress with the TEM images.

Figure 6 (a)~(d) present the superimposed stress contours of the peak stress (absolute value) on top of the TEM images. Two sets of images, samples B(ii) and C(ii), are used to depict the results for scratches in the direction of [110] and [010] respectively. Each set contains two identical TEM images, with the left denoting the superimposed $\tau_{(-11-1)[110]}$ and the right denoting superimposed $\tau_{(1-1-1)[110]}$. Fig. 6 (e)~(h) are schematic illustrations of Fig. 6 (a)~(d) showing a strong correlation between the slip band and the localized shear stress in Fig. 6 (a)~(d).

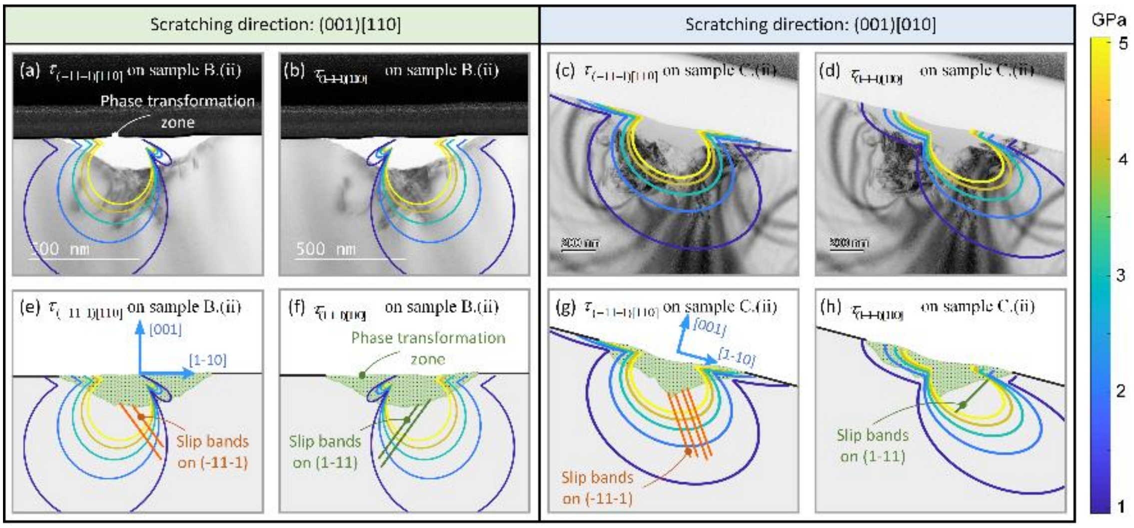


Figure 6. Contours of shear stress (absolute values) $\tau_{(-11-1)[110]}$ and $\tau_{(1-1-1)\ [110]}$ superimposed on top of the TEM images (a)(b)(c)(d) and corresponding schematics (e)(f)(g)(h) demonstrating the robust correlation between the slip band and shear stress.

The contours in Fig. 6 (a) and Fig. 6 (b) are axisymmetric, as $\tau_{(-11-1)[110]}$ and $\tau_{(1-1-1)[110]}$ are symmetric with respect to the cutting direction of [110]. The same contour lines were used for all the stress contours in Fig. 6. It is clear from Fig. 6 that slip bands terminates halfway between the first and second contour lines, despite each sample corresponding to a different normal load and cutting direction. This demonstrates a strong correlation between the depth of damage and the magnitude of the shear stress, which qualitatively verifies of the hypothesis in terms of dislocation distribution. The theoretically resolved critical shear stress was further benchmarked with the experimental results obtained both in this paper and previously reported works [14]. These critical stress values are summarized in Table 2. The data indicates that the critical resolved shear stresse $\tau_{\{111\}<110>}$ was within the range of 1.5±0.5 GPa with an approximate minimum magnitude of 1 GPa.

Table 2: Shear stresses at the dislocation termination point in the test samples

| Sample | Scratch tip | Direction | Normal load (mN) | Velocity | Minimun shear stress at dislocation position (GPa) |
|---|---|---|---|---|---|
| A(i) | Berkovich | (001)[110] | 0.5 | 0.1 m/s | 1.4 |
| A(ii) | Berkovich | (001)[110] | 3.2 | 0.1 m/s | 1.1 |
| B(i) | Berkovich | (001)[110] | 1.8 | 1 m/s | 1.2 |
| B(ii) | Berkovich | (001)[110] | 5.2 | 1 m/s | 1.9 |
| C(i) | Berkovich | (001)[010] | 2.2 | 1 m/s | 1.6 |
| C(ii) | Berkovich | (001)[010] | 4.6 | 1 m/s | 1.7 |
| Huang(i)[37] | Conical | (001)[110] | 2 | 0.4 μm/s | 1.2 |
| Huang(ii)[37] | Conical | (001)[110] | 4 | 0.4 μm/s | 1.3 |
| Huang(iii)[37] | Conical | (001)[110] | 6 | 0.4 μm/s | 1.3 |

The same argument explains the variations in the dislocation distribution along different scratching directions as shown in Fig. 3 and Fig. 6. The main observations were (i): In [110] scratches, the slip bands are symmetrically distributed in an 'X' pattern due to axisymmetric shear stresses of $\tau_{(-11-1)[110]}$ and $\tau_{(1-1-1)[110]}$ and slip planes of (-11-1) and (1-1-1). (ii) In [010] scratches, slip bands on (-11-1) planes shifted to the other side of the scratch opposite to that in the [110] scratches, as the stress contour changes. The deformation area at the bottom left of the scratch in the TEM images is due to slip bands on the (11-1) planes, in accordance with the symmetric nature of the four {111} slip planes, which would be easier to understand when viewed in conjunction with Figure 5. (iii) In [010] scratches, the contrast characteristics of the slip bands on the left and right sides of the bottom of the scratch in the TEM image are different because the electron incidence direction [110] in this study is not parallel to the (11-1) planes. These observations provide strong evidence that supports the hypothesis of this investigation, which states that the shear stress acting on a dislocation line in the slip plane determines the position and extent of dislocations in single-crystal materials.

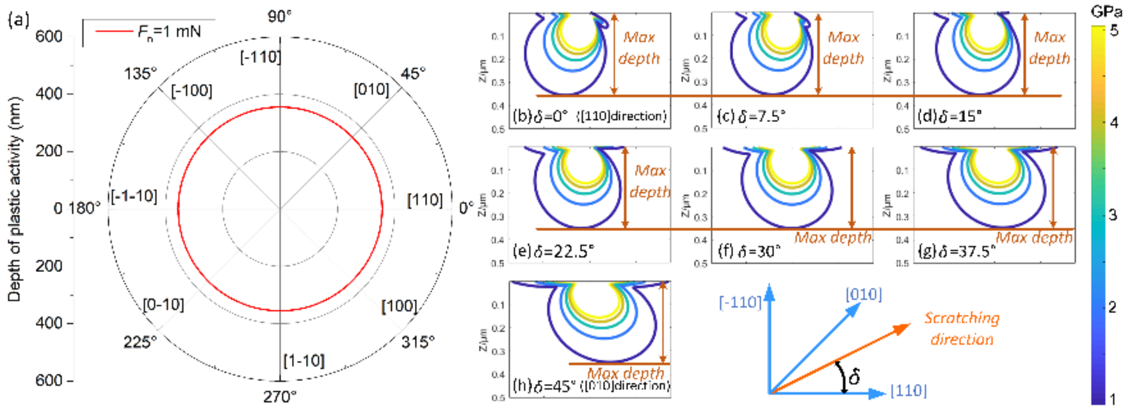


Figure 7. Maximum depth of (a) plastic activity vs. scratch direction and (b) contours of shear stress $\tau_{(-11-1)[110]}$ indicating maximum dislocation depth as the scratch direction angle δ ranges from 0~45°.

**Error! Reference source not found.** plots the dislocation depth as a function of scratch d irection for a given normal load through the stress contours of scratch direction δ in the range of 0~45°, considering the symmetry of the slip planes illustrated in Figure 5. **Error! R eference source not found.** shows that a change in the direction of scratching leads to a variation in the shape of the stress contour, which in turn changes the distribution of dislocations. Specifically, it illustrates that the distribution of shear stress (stress contours) is direction-dependent, leading to certain cutting directions being "easy" and others "hard" depending on the crystallographic orientation. Surprisingly, this change does not alter the theoretical maximum depth of dislocations.

Based on the above analyses, an empirical model of the maximum dislocation depth as a function of the normal load was fitted considering the complexity of the shear stress analysis:

$$d = k_0 F_n^{k_1}, k_0 = 355\mathrm{nm/mN^{1/2}}, k_1 = 0.5 \quad (8)$$

where $d$ is the maximum dislocation depth, $F_n$ is the normal load and coefficient $k_0$ $k_1$ are fitted to be 355 nm/mN$^{1/2}$ and 0.5 respectively.

Figure 8(a) establishes the maximum dislocation depth in single-crystal silicon with respect to the scratch normal load. The diagrams together with **Error! Reference source not found.** provide visual representation of how the distribution and strength of shear stress affects the formation of dislocations at different directions, with comparison to the predicted maximum dislocation depth from the critical shear stress criterion.

Two key observations can be made from Figure 8: (i) All experimental results are below the theoretical predictions as expected, especially for the [110] scratches. (ii) The dislocation depth of the [010] scratch is slightly larger than that of the [110] scratch, despite the theoretically predicted maximum depths for these two groups being the same. Both of these phenomena are reasonable because the increase in shear stress $\tau$ will result in an exponential increase in the nucleation rate [15]. Therefore, the higher stresses within the yellow stress contour promote a greater possibility for nucleation and thus dislocations tends to originate within the area of yellow stress contour where the corresponding depth of critical resolved shear stress is smaller than the predicted maximum dislocation depth, as schematically illustrated in Figure 8(b)~(c). The same argument also explains the differences between the [110] and [010] scratches. The depth of critical resolved shear stress corresponding to the area which promotes dislocation nucleation the most in the [110] scratch is smaller than that of the [010] scratch due to differences in the shape of stress contours. This study also observed no significant effects of velocity on the dislocation depth.

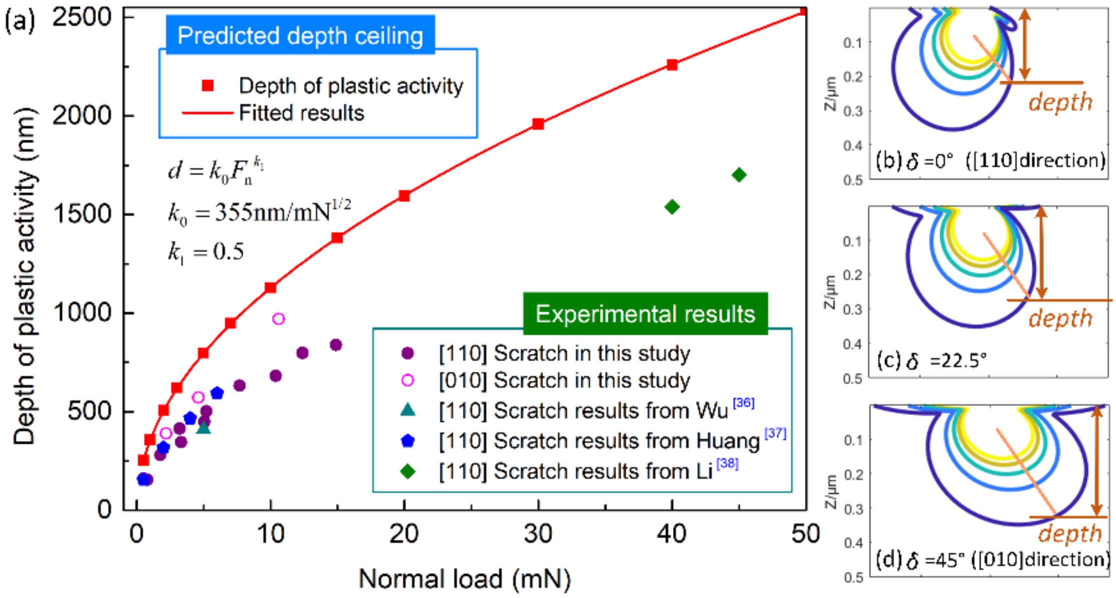


Figure 8. (a) Maximum depth of plastic activity vs. normal load obtained from scratch tests in silicon. The red dots and fitted lines denote the predicted maximum dislocation depth according to the proposed critical shear stress criterion. The scatter plots represent experimental data from this study and previously published works [36][37][38]. (b)~(c) are schematic diagrams of shear stress contours at different scratch directions, which explains why experimental results are below the theoretical predictions and why the dislocation depth of the [010] scratch is a bit larger than that of the [110] scratch.

### *3.3 Depth of phase transformed layer*

As can be seen in Figure 2, the diffraction pattern indicates that the region undergoing phase transformation is composed of amorphous silicon (a-Si) but may also include the formation of growing nanocrystals at deeper penetration depths. The transformed layer forms at the top surface and has an irregular interface between amorphous and crystalline silicon, which is a result of the anisotropy of silicon's atomic lattice structure.

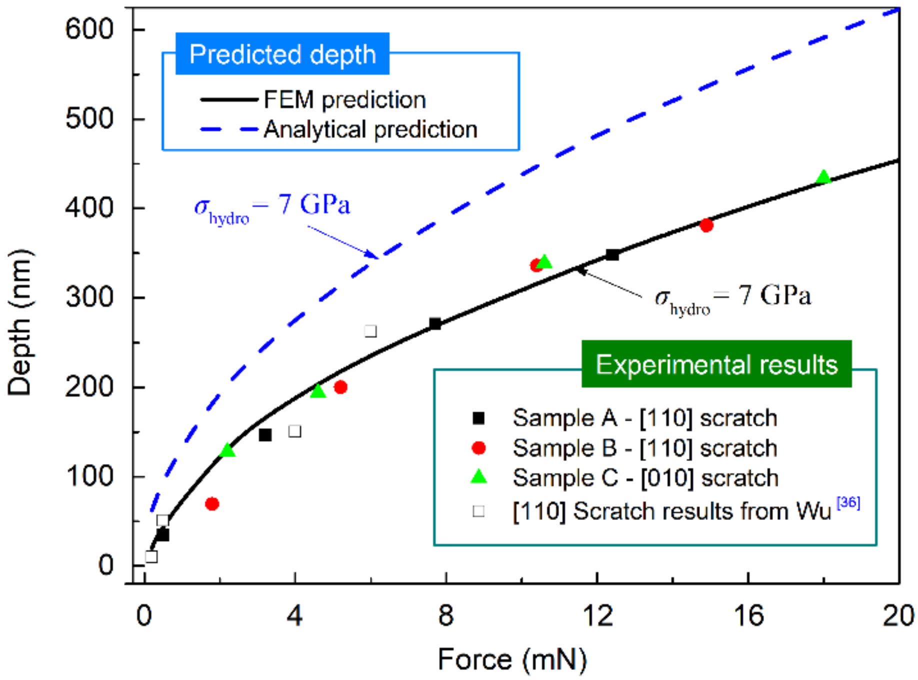


Figure 9. Depth of phase transformed layer as a function of normal load predicted by the critical hydrostatic stress criterion by analytical and FEM method respectively. Scatter plots denote experimental data from this study and previously published works [36].

By analyzing the TEM results of scratched samples, the scatter plot in **Error! Reference source not found.** shows the variation of the depth of the phase transformed layer with the applied scratch load. According to previous research, the occurrence of phase transformation is closely linked to hydrostatic pressure, which led us to propose that the depth of the phase transformed layer can be predicted by calculating the hydrostatic pressure from the applied load. However, previous studies have reported different values for the critical hydrostatic pressure at which the high pressure phase transformation (HPPT) from Si-I to Si-II takes place, ranging from 5.0-8.5 GPa [39], 11.3-12.5 GPa [40], and 9-16 GPa [37]. To determine the critical stress applicable to scratching, we estimated the hydrostatic stress in the deformation region and plotted the depth corresponding to the critical stress in **Error! Reference source not found.**.

It is important to note that in this paper, the finite element method (FEM, as discussed in Appendix B) was used to determine the critical stress value for phase transformation, instead of the analytical method based on Eq. (2). This choice was made for several reasons: (i) using the point loading assumption in the analytical solution would result in errors in the calculation as the depth decreases towards zero, due to the equations used for stress calculations (see Appendix A); (ii) Furthermore, point loading implies that the contact area is not considered in the analytical calculations, whereas in the calculation of the stress distribution in the phase transformed layer, the contact area may have a strong effect on the calculation results due to the small depth of the phase transformed layer. Therefore, it is considered that the finite element results are more suitable. After specifying the stress threshold, the analytical method based on Eq. (2) was also employed as a comparison to calculate the predicted depth at this threshold stress, leading to the discussion of the following two issues in this section: (i) of the various phase transformation hydrostatic stress thresholds reported previously, which stress value is applicable to the experimental results in this study? (ii) with the critical hydrostatic stress value determined by FEM method, can the analytical method still be used to predict the depth of the phase transformed layer?

The high degree of agreement between the FEM-based prediction results and the experimental results in **Error! Reference source not found.** suggests that the depth of t he phase transformed layer can be accurately predicted from the applied load using the hydrostatic stress criterion, with a stress threshold of approximately 7 GPa. However, the analytical method's predictions deviate significantly from both the experimental results and FEM-based predictions under the same stress conditions, which is reasonable given that the analytical method does not take into account the contact area of the indenter, unlike the FEM. This highlights the limitations of the analytical method in calculating the stress field in the near-surface region, due to its simplification of the point load. Therefore, it is considered unacceptable to use the results of the analytical method to predict the depth of the phase transformed layer. The experimental results do not indicate any effect of scratch direction or velocity on the depth of the phase transformed layer.

### *3.4 Depth of median crack*

As the indentation load increases, microcracks begin to appear at the intersection of defects. This can be observed clearly in the sub-surface in Figure 2. Many analytical models that are used to predict crack depth in hard, brittle materials are based on fracture mechanics theory, such as the widely used Lambropoulos model [19]. This model establishes the relationship between median crack depth (dms) and normal force as follows:

$$d_{ms} = 0.206\left(\frac{E}{H}\right)^{1/3}(\cot\varphi)^{4/9}\left(\frac{F_n}{K_c}\right)^{2/3} \tag{9}$$

where $E$, $H$, $F_n$ and $K_c$ are the Young’s modulus, hardness, normal load and fracture toughness, and $\varphi$ is half included angle of the tool respectively.

For scratch tests performed on silicon (with Young's modulus of E = 130 GPa [41], Hardness of H = 13 GPa [41], Critical angle of Φ = 72.5°, Critical stress intensity of Kc = 1 MPa m1/2 [41]) in this study, Fig. 10 shows the predicted crack depth as a function of normal load according to the theoretical model, as well as the experimental results for two different scratch velocities and scratch directions. Similar to the results of the phase transformation depth analysis, the depth of the median crack is not influenced by the scratch velocity or direction. The comparison of the experimental results with the theoretical predictions indicates that the model proposed by Lambropoulos [19] holds valid within the scope of this study.

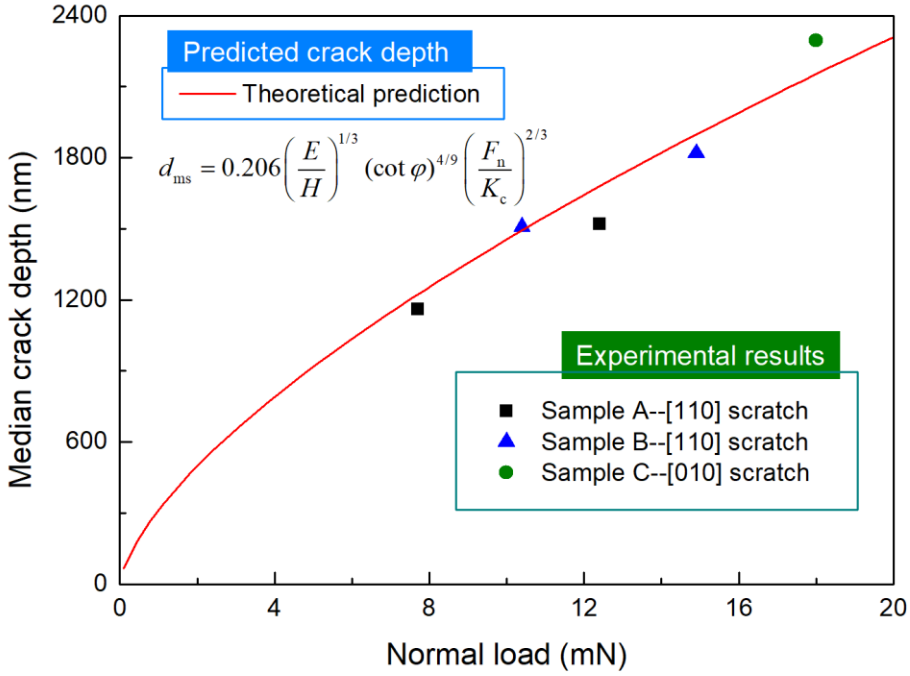


Figure 10. Sub-surface crack depth as a function of normal load predicted by the analytical model [19]. The symbols in the graph denote the experimental values freshly obtained in this paper.

It is worth noting that sample C has the highest normal load corresponding to the first appearance of median crack among the three groups of samples. This is consistent with previous qualitative research suggesting that the [100] direction has more plasticity and ductility than the [110] direction on the (001) cubic face [42].

Additionally, an interesting phenomenon was observed in the [110] scratches with median cracks, as an increase in load shifts the angle of the crack from a low Miller index to a high Miller index, as shown in Figure 2. This phenomenon has also been observed during indentation experiments [12] on single-crystal silicon and can be explained using the theory of fracture mechanics. The fracture toughness of single-crystal silicon is higher in the direction of high Miller index [41]. Thus, a crack in the direction of high Miller index consumes more energy, therefore, at higher loads, a change in the crack angle becomes more energetically favorable.

### *3.5 Width of the inelastic zone*

The width of the inelastic zone of the scratch can be directly measured from cross-sectional TEM micrographs of the scratch (Fig. 6). The results show that the width of the inelastic region is equivalent to that of the phase transformation region under smaller loads. As the load increases and clusters of crystal defects form at the bottom of the phase transformed region, some crystal defects may occasionally extend to both sides of the groove. Due to the random nature of crystal defect propagation, the width of the inelastic zone becomes slightly larger than the phase transformed region. However, given the shallow subsurface damage depth in the ductile-regime grinding and the simplicity of measuring the scratch feature, the width of the phase transformed region on the scratch surface was used as the inelastic region size during the silicon scratching process in this study.

Based on this simplification, an AFM was used to measure the dimensions of the inelastic zone of the scratch. Earlier, Figure 2 presented AFM topography and phase micrographs of [110] scratches. Variations in the phase images typically indicate changes in the surface properties of the sample. Since phase transformation of single-crystal silicon alters the mechanical properties of the deformed material (e.g., elastic modulus), it is reasonable to assume that the width of the scratch in the AFM phase image corresponds to the width of the inelastic region on the surface of the scratch. To facilitate comparison between the inelastic zone size measured by the TEM and AFM, the location of the AFM measurement was aligned with where the FIB-TEM sample was prepared.

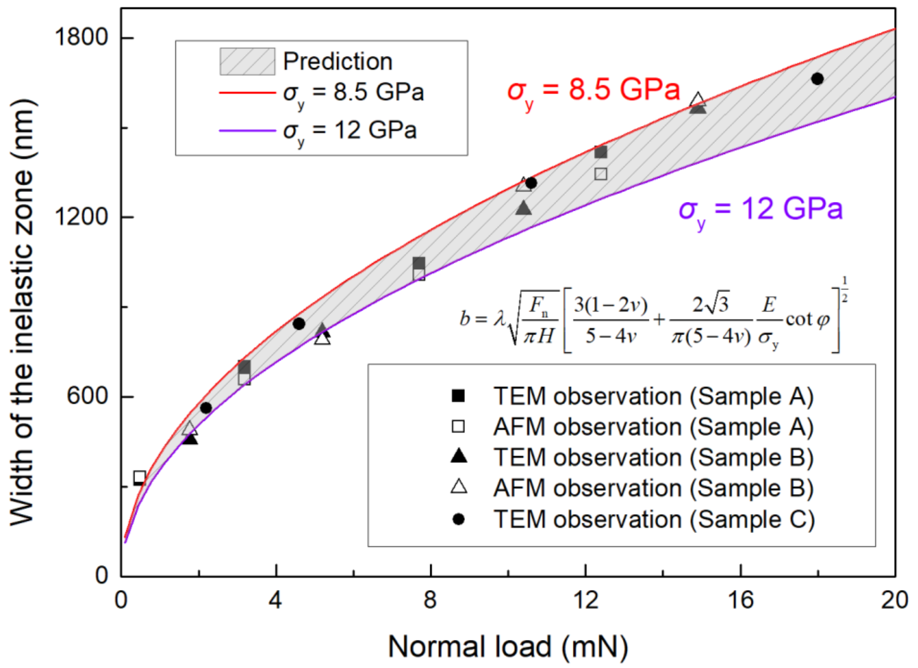


Figure 11. Inelastic zone width as a function of normal load predicted by the analytical model [20]. The scatters represent the experimental results of this paper.

The measured width of the inelastic zone is shown in Figure 11. The slight deviations between these two measurement methods can be attributed to the measurement error of the AFM phase image and the measurement position error of the two methods. Figure 11 shows that the AFM phase images can be used as a substitute for the costly TEM test when evaluating the width of the inelastic zone for single-crystal silicon scratches.

Jing *et al.* [20] analytically predicted the size of inelastic regions during scratching using the ECCM model in indentation, due to its similarity to the scratching process. The formula is as follows:

$$b = \lambda \sqrt{\frac{F_{\mathrm{n}}}{\pi H}} \left[ \frac{3(1-2v)}{5-4v} + \frac{2\sqrt{3}}{\pi(5-4v)} \frac{E}{\sigma_{\mathrm{y}}} \cot\varphi \right]^{\frac{1}{2}} \quad (10)$$

where $\sigma_y$ is the yield strength, λ is a dimensionless parameter determined by the geometry of the indenter, and $v$ is the Poisson's ratio. Eq. (10) reveals the relationship between the plasticity zone width and the normal force, tool geometry, and material property parameters. For single-crystal silicon, with a Poisson's ratio v of 0.28 and yield stress $\sigma_y$ in the range of 8.5 to 12 GPa [43][44][45], the inelastic zone width as a function of normal load was predicted as the shaded area in Figure 11. The theoretical prediction interval can cover the experimental results well and thus visually confirms the applicability of the Jing's model in the scratching process of single-crystal silicon, that is, the size of the inelastic region is proportional to the square root of the normal load.

The agreement of the experimental results with the theoretical predictions was unexpected because the scratching experiments were performed at scratching velocities of 0.1 m/s and 1 m/s, while the model proposed by Jing *et al.* [20] was developed from the quasistatic indentation tests. It is well-known that the scratch load is positively correlated with the scratch velocity for the same contact area due to the strain rate hardening [46]. The reason why the model is still applicable to single-crystal silicon scratching is that the normal force determines the inelastic zone size of single-crystal silicon during the scratching process for a given tool geometry. Therefore, the effect of scratch velocity on the width is not visible in Figure 11 where the horizontal coordinate denotes the normal load. In addition, the experimental data points from different scratch velocities are clustered on the same curve in Figure 11, indicating that the scratching velocity has little influence on the relationship between the size of the inelastic zone and the normal force, which further justifies the above analysis.

## 4. Conclusions

The existing analytical models available for predicting sub-surface damage depth, critical crack length and the width of inelastic region during its contact loading are based on a significant assumption that the materials are isotropic. A wide variety of engineering materials such as silicon, silicon carbide and diamond used in advanced engineering applications, particularly in the optics and electronics industries are anisotropic and hence, the existing theories cannot be used to readily explain the direction dependent plasticity observed in most sub-surface studies using TEM. This paper proposes a novel shear stress-based criterion to predict the sub-surface damage depth hitherto not reported in the extant literature. The results not only fully demonstrate the feasibility of using the stress field and the appropriate stress criterion to calculate the depth of damage but also revealed the physical mechanisms governing the differences in the deformation at different scratch speeds. In addition, the applicability of inelastic, plastic and median cracking (phase transformation and crack depth) prediction models developed from indentation theory in scratching tests has been also compared. The main findings of the paper were summarised as follows:

1. Critically resolved shear stress on the slip planes along the direction of Burgers vector can be used to predict both the depth and distribution of dislocations in the sub-surface in silicon as well as the slip bands. In this study, scratch tests were performed on the (001) orientation along the [110] and [010] direction and it was found that the shear stress $\tau_{\{111\}<110>}$ where the dislocation terminates was of the order of 1.5±0.5 GPa. The stress contours congruently overlaid on the TEM images revealed a distinct boundary that limits the travel of a propagated dislocation. In

other words, our newly proposed stress based model suggested a pathway for experimental quantification of the post deformation TEM microscopic images.

2. The phase transformation depth, crack depth, and the width of inelastic zone, as functions of normal load, were found to be insensitive to changes in the scratch direction, with the exception of dislocation depth and distribution. Only the stress criterion related to crystal orientation needs to take the scratch direction into consideration.
3. Due to the close proximity of the phase transformed layer to the contact zone, there is considerable discrepancy in the prediction of the depth of the phase transformed layer by the Boussinesq stress field for a point load, whereas the finite element method, which takes into account the contact area, is able to predict it accurately.

## Acknowledgments

All authors appreciate the financial support from the National Natural Science Foundation of China (51875078, 51991372, 51975094), and the Science Fund for Creative Research Groups of NSFC of China (51621064).

SG would like to acknowledge the financial support provided by the UKRI via Grants No. EP/S036180/1 and EP/T024607/1, a feasibility study award to LSBU from the UKRI National Interdisciplinary Circular Economy Hub (EP/V029746/1), Hubert Curien Partnership Programme from the British Counsil and the International exchange Cost Share award by the Royal Society (IEC\NSFC\223536). Wherever applicable, the work made use of Isambard Bristol, UK supercomputing service accessed by a Resource Allocation Panel (RAP) grant as well as ARCHER2 resources (Project e648).

Ning would like to extend his heartfelt gratitude to Yunxiang Lu for his invaluable assistance in the creation of this paper.

# Appendix A

$$\alpha_{xx}(x,y,z)=\frac{P}{2\pi}\left\{\frac{1-2v}{r^2}\left[\left(1-\frac{z}{\rho}\right)\frac{x^2-y^2}{r^2}+\frac{zy^2}{\rho^3}\right]-\frac{3zx^2}{\rho^5}\right\} \tag{A-1}$$

$$\alpha_{yy}(x,y,z)=\frac{P}{2\pi}\left\{\frac{1-2v}{r^2}\left[\left(1-\frac{z}{\rho}\right)\frac{y^2-x^2}{r^2}+\frac{zx^2}{\rho^3}\right]-\frac{3zy^2}{\rho^5}\right\} \tag{A-2}$$

$$\alpha_{zz}(x,y,z)=-\frac{3P}{2\pi}\frac{z^3}{\rho^5} \tag{A-3}$$

$$\alpha_{xy}(x,y,z)=\frac{P}{2\pi}\left\{\frac{1-2v}{r^2}\left[\left(1-\frac{z}{\rho}\right)\frac{xy}{r^2}-\frac{xyz}{\rho^3}\right]-\frac{3xyz}{\rho^5}\right\} \tag{A-4}$$

$$\alpha_{yz}(x,y,z)=-\frac{3P}{2\pi}\frac{yz^2}{\rho^5} \tag{A-5}$$

$$\alpha_{zx}(x,y,z)=-\frac{3P}{2\pi}\frac{xz^2}{\rho^5} \tag{A-6}$$

$$\beta_{xx}(x,y,z)=\frac{P}{2\pi}\left\{(1-2v)\left[\frac{x}{\rho^3}-\frac{3x}{\rho(\rho+z)^2}+\frac{x^3}{\rho^3(\rho+z)^2}+\frac{2x^3}{\rho^2(\rho+z)^3}\right]-\frac{3x^3}{\rho^5}\right\}$$

(A-7)

$$\beta_{yy}(x,y,z)=\frac{P}{2\pi}\left\{(1-2v)\left[\frac{x}{\rho^3}-\frac{x}{\rho(\rho+z)^2}+\frac{xy^2}{\rho^3(\rho+z)^2}+\frac{2xy^2}{\rho^2(\rho+z)^3}\right]-\frac{3xy^2}{\rho^5}\right\}$$

(A-8)

$$\beta_{zz}(x,y,z)=-\frac{P}{2\pi}\frac{3xz^2}{\rho^5} \tag{A-9}$$

$$\beta_{xy}(x,y,z)=\frac{P}{2\pi}\left\{(1-2v)\left[-\frac{y}{\rho(\rho+z)^2}+\frac{x^2y}{\rho^3(\rho+z)^2}+\frac{2x^2y}{\rho^2(\rho+z)^3}\right]-\frac{3x^2y}{\rho^5}\right\}$$

(A-10)

$$\beta_{yz}(x,y,z) = -\frac{P}{2\pi}\frac{3xyz}{\rho^5} \quad \text{(A-11)}$$

$$\beta_{zx}(x,y,z) = -\frac{P}{2\pi}\frac{3x^2z}{\rho^5} \quad \text{(A-12)}$$

where $r^2=x^2+y^2$ and $\rho^2= x^2+y^2+z^2$, $P$ the normal load and $v$ Poisson's ratio of the material.

## Appendix B

In this study, an indentation finite element model was implemented in the commercial ABAQUS software. Fig. B-1 shows the finite element model for a two-dimensional specimen of 1.0×1.0 μm$^2$. The two-dimensional geometry enables an efficient calculation by reducing the number of numerical operations. The indenter is defined as a sphere and is free to move only in the vertical direction. The curvature of the indenter is 850 nm and is the result of careful measurements, which are reported in our previous paper [26]. The silicon workpiece ($E$ = 130 GPa [41], $v$ = 0.28) was segmented into a 5 nm grid size consisting of 20,000 four-node axisymmetric elements (CAX4R). Rigid walls were used as the boundary of the workpiece as silicon is a hard material and the bottom of the specimen was completely fixed to prevent it from moving.

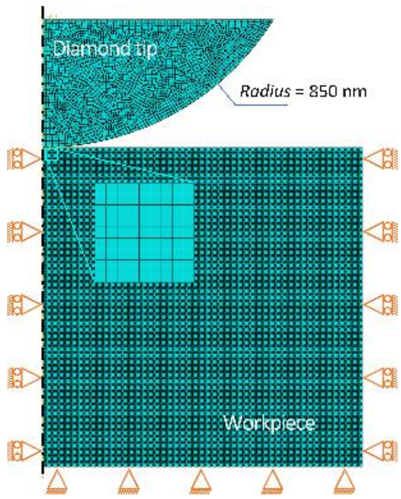


Figure B-1. FEM simulation model

Before simulation, the following assumptions are made in the present work:

(i) The diamond tip is considered to be a rigid body. The material of the indenter tip is diamond, which is much stronger and harder than those of silicon. Only slight elastic deformation occurs in the diamond tip.

(ii) Indentation was used to calculate the hydrostatic pressure under normal load during the scratching process. Analytical calculations based on Eq. (2) show that the tangential load has a negligible effect on the hydrostatic pressure distribution directly below the diamond tip.

(iii) Only the material elasticity is considered. The TEM results show that the spring-back of the material under small loads is very significant.

The simulation results are demonstrated in Fig. B-2. The stress field is asymmetric, and the results are shown at the plane of symmetry.

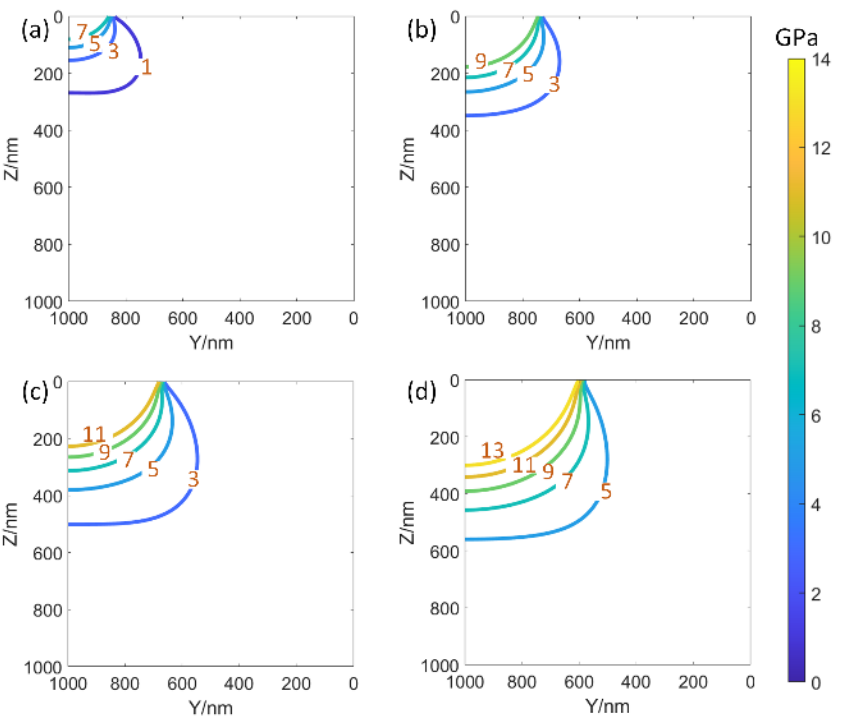


Figure B-2. Hydrostatic stress (GPa) field in the workpiece at a normal load of (a) 1 mN, (b) 5 mN, (c) 10 mN, and (d) 20 mN, respectively.

## References

[1] https://www.marketwatch.com/press-release/silicon-wafer-market-2022-qualitative-research-cagr-analysis-global-growth-opportunities-developing-strategies-top-key-players-and-size-forecast-to-2027-2022-08-11 Accessed 24th Aug 2022

[2] Pan Y, Zhou P, Yan Y, Pan, Y, Zhou P, Yan Y, Agrawal A, Wang Y, Guo D, Goel S. New insights into the methods for predicting ground surface roughness in the age of digitalisation. Precis Eng., 2020.

[3] Marks M R, Hassan Z, Cheong K Y. Ultrathin wafer pre-assembly and assembly process technologies: A review. Crit. Rev. Solid State Mater. Sci., 2015, 40(5): 251-290.

[4] Goel S, Luo X, Agrawal A, Reuben R L. Diamond machining of silicon: a review of advances in molecular dynamics simulation. Int. J. Mach. Tools Manuf., 2015, 88: 131-164.

[5] S.Z. Chavoshi, S. Xu, S. Goel, Addressing the discrepancy of finding the equilibrium melting point of silicon using molecular dynamics simulations, Proc. Math. Phys. Eng. Sci. 2017, 473(2202)

[6] Khatri N, Barkachary B M, Muneeswaran B, Al-Sayegh R, Luo X, Goel S. Surface defects incorporated diamond machining of silicon. Int. J. Extreme Manuf., 2020, 2(4): 045102.

[7] Huang N, Yan Y, Zhou P, Kang R, Guo D, Goel S. Elastic recovery of monocrystalline silicon during ultra-fine rotational grinding. Precis Eng., 2020.

[8] Goel S, Yan J, Luo X, Agrawal, A. Incipient plasticity in 4H-SiC during quasistatic nanoindentation. J. Mech. Behav. Biomed., 2014, 34: 330-337.

[9] Chavoshi S Z, Goel S, Luo X. Influence of temperature on the anisotropic cutting behaviour of single crystal silicon: A molecular dynamics simulation investigation. J. Manuf. Process., 2016, 23: 201-210.

[10] Gassilloud R, Ballif C, Gasser P, Buerki G, Michler J. Deformation mechanisms of silicon during nanoscratching. Phys. Status Solidi A-Appl. Res., 2005, 202(15): 2858-2869.

[11] Goel S, Kovalchenko A, Stukowski A, Cross G. Influence of microstructure on the cutting behaviour of silicon. Acta Mater., 2016, 105, 464-478.

[12] Bradby J E, Williams J S, Wong-Leung J, Swain M V, Munroe P. Mechanical deformation in silicon by micro-indentation. J. Mater. Res., 2001, 16(5): 1500-1507.

[13] Zhou L, Tian Y B, Huang H, Sato H, Shimizu J. A study on the diamond grinding of ultra-thin silicon wafers. Proc. Inst. Mech. Eng. Part B-J. Eng. Manuf., 2012, 226(1): 66-75.

[14] Wu Y Q, Huang H, Zou J, Zhang L C, Dell J M. Nanoscratch-induced phase transformation of monocrystalline Si. Scr. Mater., 2010, 63(8): 847-850.

[15] Chen M, Pethö L, Sologubenko A S. Achieving micron-scale plasticity and theoretical strength in Silicon. Nat. Commun., 2020, 11, 2681.

[16] Fang Q H, Zhang L C. Prediction of the threshold load of dislocation emission in silicon during nanoscratching. Acta Mater., 2013, 61(14): 5469-5476.

[17] Wu, Hao. Fundamental investigations of cutting of silicon for photovoltaic applications. Diss. Georgia Institute of Technology, 2012.

[18] Johnson K L. Contact mechanics. Cambridge university press, 1987.

[19] Lambropoulos J C, Jacobs S D, Ruckman J. Material removal mechanisms from grinding to polishing. Ceram. Trans., 1999, 102: 113-128.

[20] Jing X, Maiti S, Subhash G. A new analytical model for estimation of scratch-induced damage in brittle solids. J. Am. Ceram. Soc., 2007, 90(3): 885-892.

[21] Zhang L, Chen P, An T, Dai Y, Qin F. Analytical prediction for depth of subsurface damage in silicon wafer due to self-rotating grinding process. Curr. Appl. Phys., 2019, 19(5): 570-581.

[22] Dong Z, Cheng H. Developing a trend prediction model of subsurface damage for fixed-abrasive grinding of optics by cup wheels. Appl. Opt., 2016, 55(32): 9305-9313.

[23] Li H N, Yu T B, Zhu L D, Wang W S. Analytical modeling of grinding-induced subsurface damage in monocrystalline silicon. Mater. Des., 2017, 130: 250-262.

[24] Wang P, Ge P, Bi W, Liu T, Gao Y. Stress analysis in scratching of anisotropic single-crystal silicon carbide. Int. J. Mech. Sci, 2018, 141: 1-8.

[25] Li L, Ge P. Analytical modeling of the stress field in scratching anisotropic single-crystal silicon. Mater. Sci. Semicond. Process, 2022, 152: 107099.

[26] Huang N, Yan Y, Zhou P, Kang R, Guo D. Elastic-plastic deformation of single-crystal silicon in nano-cutting by a single tip tool. Jpn. J. Appl. Phys., 2019, 58(8): 086501.

[27] Kovalchenko A M, Goel S, Zakiev I M, Pashchenko E A, Al-Sayegh R. Suppressing scratch-induced brittle fracture in silicon by geometric design modification of the abrasive grits. J. Mater. Res. Technol., 2019, 8(1): 703-712.

[28] Tang F, Zhang L. Subsurface nanocracking in monocrystalline Si (0 0 1) induced by nanoscratching. Eng. Fract. Mech., 2014, 124: 262-271.

[29] Nabarro F R N. Fifty-year study of the Peierls-Nabarro stress. Mater. Sci. Eng. A, 1997, 234: 67-76.

[30] Meyers M A, Chawla K K. Mechanical behavior of materials. Cambridge university press, 2008.

[31] Danilewsky A N, Wittge J, Croell A, Allen D, McNally P, Vagovič P, Garagorri J. Dislocation dynamics and slip band formation in silicon: In-situ study by X-ray diffraction imaging. J. Cryst. Growth, 2011, 318(1): 1157-1163.

[32] Hänschke D, Danilewsky A, Helfen L, Hamann E, Baumbach T. Correlated three-dimensional imaging of dislocations: Insights into the onset of thermal slip in semiconductor wafers. Phys. Rev. Lett, 2017 Nov 20;119(21):215504.

[33] Huang J Y, Ponce F A, Caldas P G, Prioli R, Almeida C M. The effect of nanoscratching direction on the plastic deformation and surface morphology of InP crystals. Int. J. Appl. Phys, 2013 Nov 28;114(20):203503.

[34] Cook R F, Pharr G M. Direct observation and analysis of indentation cracking in glasses and ceramics. J. Am. Ceram. Soc., 1990, 73(4): 787-817.

[35] Mizushima Y, Kim Y, Nakamura T, Mizushima Y, Kim Y, Nakamura T, Sugie R, Hashimoto H, Uedono A, Ohba T. Impact of back-grinding-induced damage on Si wafer thinning for three-dimensional integration. Jpn. J. Appl. Phys., 2014, 53(5S2): 05GE04.

[36] Wu L, Chen P, Deng L, Zhang P, Yu B, Qian L. Effects of crystal planes on topography evolution of silicon surface during nanoscratch-induced selective etching. Mater. Sci. Semicond. Process, 2021 Mar 15;124:105606.

[37] Han H. Ductile grinding of brittle materials, ISAAT2021.

[38] Xuliang L. Brittle-to-ductile transition mechanism of single crystal silicon induced by nanoscratching, ISAAT2021.

[39] Domnich V, Gogotsi Y, Dub S. Effect of phase transformations on the shape of the unloading curve in the nanoindentation of silicon. Appl. Phys. Lett., 2000, 76(16): 2214-2216.

[40] Hu J Z, Merkle L D, Menoni C S, Spain I L. Crystal data for high-pressure phases of silicon. Phys. Rev. B, 1986, 34(7): 4679.

[41] Ebrahimi F, Kalwani L. Fracture anisotropy in silicon single crystal. Mater. Sci. Eng. A, 1999, 268(1-2): 116-126.

[42] O'Connor B P, Marsh E R, Couey J A. On the effect of crystallographic orientation on ductile material removal in silicon. Precis. Eng., 2005, 29(1): 124-132.

[43] Domnich V, Gogotsi Y. Phase transformations in silicon under contact loading. Rev. Adv. Mater. Sci., 2002, 3(1): 1-36.

[44] Zhang L, Tanaka H. Atomic scale deformation in silicon monocrystals induced by two-body and three-body contact sliding. Tribol. Int., 1998, 31(8): 425-433.

[45] Hong Y, Zhang N, Xiong L. Nanoscale plastic deformation mechanisms of single crystalline silicon under compression, tension and indentation. J. Micromech. Mol. Phys., 2016, 1(03n04): 1640007.

[46] Johnson G R, Cook W H. A constitutive model and data for metals subjected to large strains, high strain rates and high temperatures. Proceedings of the 7th International Symposium on Ballistics. 1983, 21(1): 541-547.

# Figure captions

Figure 1. Schematic illustration of the scratch method (a)~(c) showing wear traces with nanoscale ramping depth-of-cut and the sample preparation method (d) denoting the area on the scratched region being chosen for the cross-sectional TEM observation.

Figure 2. Scratch topographies inspected by AFM under tapping mode and corresponding detailed TEM observations of subsurface defects in specimens A, B, and C. The scratches are numbered as A.(i)~A.(iv), B.(i)~B.(iv) and C.(i)~ C.(iv) to clearly show the TEM micrographs at various loads.

Figure 3. Schematics of scratch groove sub-surface structure in (a) conventional expanding cavity model, (b) [110] scratch in single-crystal silicon and (c) [010] scratch in single-crystal silicon. Solid lines in (b) and (c) denote slip bands on {111} slip planes viewed edge-on and dashed and dotted lines in (c) denote slip bands on {111} slip planes oblique to the [110] projection.

Figure 4. Schematic of (a) formation of slip bands from dislocation loops during scratching and (b) multiplication and propagation of dislocation loops on the {111} slip plane. Each half loop consists of two inclined 60° and one screw dislocation with a Burgers vector orientation of <110>.

Figure 5. Schematics of (a) coordinate *XYZ* denoted by crystal orientation, (b)-(c) coordinate transformation, and (d) overview of three coordinate systems. The stress field $\boldsymbol{\sigma}$ is first transformed from the scratch coordinate system $X''Y''Z''$ to a fixed intermediate coordinate system *XYZ* by rotating it by an angle $\delta$ around the $Z''$ axis, which is followed by a rotation around the $X$ axis by angle $\eta$, resulting in the transformed coordinate system $X'Y'Z'$.

Figure 6. Contours of shear stress (absolute values) $\tau_{(-11-1)[110]}$ and $\tau_{(1-1-1)\,[110]}$ superimposed on top of the TEM images (a)(b)(c)(d) and corresponding schematics (e)(f)(g)(h) demonstrating the robust correlation between the slip band and shear stress.

Figure 7. Maximum depth of (a) plastic activity vs. scratch direction and (b) contours of shear stress $\tau_{(-11-1)[110]}$ indicating maximum dislocation depth as the scratch direction angle δ ranges from 0~45°.

Figure 8. (a) Maximum depth of plastic activity vs. normal load obtained from scratch tests in silicon. The red dots and fitted lines denote the predicted maximum dislocation depth according to the proposed critical shear stress criterion. The scatter plots represent experimental data from this study and previously published works [36][37][38]. (b)~(c) are schematic diagrams of shear stress contours at different scratch directions, which explains why experimental results are below the theoretical predictions and why the dislocation depth of the [010] scratch is a bit larger than that of the [110] scratch.

Figure 9. Depth of phase transformed layer as a function of normal load predicted by the critical hydrostatic stress criterion by analytical and FEM method respectively. Scatter plots denote experimental data from this study and previously published works [36].

Figure 10. Subsurface crack depth as a function of normal load predicted by the analytical model [19]. The symbols in the graph denote the experimental values freshly obtained in this paper.

Figure 11. Inelastic zone width as a function of normal load predicted by the analytical model [20]. The scatters represent the experimental results of this paper.

# Tables

Table 1 Experimental parameters

| Sample | Velocity (m/s) | Scratch direction | Number of scratches |
|---|---|---|---|
| A | 0.1 | (001)[110] | 4 |
| B | 1 | (001)[110] | 4 |
| C | 1 | (001)[010] | 4 |

Table 2 Shear stresses at the dislocation termination point in the test samples

| Sample | Scratch tip | Direction | Normal load (mN) | Velocity | Minimun shear stress at dislocation position (GPa) |
|---|---|---|---|---|---|
| A(i) | Berkovich | (001)[110] | 0.5 | 0.1 m/s | 1.4 |
| A(ii) | Berkovich | (001)[110] | 3.2 | 0.1 m/s | 1.1 |
| B(i) | Berkovich | (001)[110] | 1.8 | 1 m/s | 1.2 |
| B(ii) | Berkovich | (001)[110] | 5.2 | 1 m/s | 1.9 |
| C(i) | Berkovich | (001)[010] | 2.2 | 1 m/s | 1.6 |
| C(ii) | Berkovich | (001)[010] | 4.6 | 1 m/s | 1.7 |
| Huang(i)[37] | Conical | (001)[110] | 2 | 0.4 μm/s | 1.2 |
| Huang(ii)[37] | Conical | (001)[110] | 4 | 0.4 μm/s | 1.3 |
| Huang(iii)[37] | Conical | (001)[110] | 6 | 0.4 μm/s | 1.3 |